Growth Kinetics of Individual Co Particles Ex-solved on SrTi$_{0.75}$Co$_{0.25}$O$_{3-\delta}$ Polycrystalline Perovskite Thin Films

Yong-Ryun Jo,[†,∥] Bonjae Koo,[‡,∥] Min-Ji Seo,[†] Jun Kyu Kim,[‡] Siwon Lee,[‡] Kyeounghak Kim,[§] Jeong Woo Han,[§] WooChul Jung,*[‡] and Bong-Joong Kim*[†]
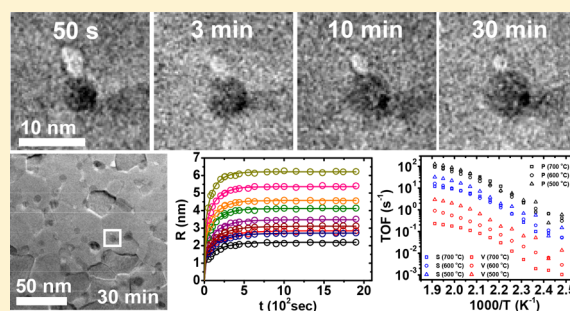
[†]School of Materials Science and Engineering, Gwangju Institute of Science and Technology (GIST), 123 Cheomdangwagi-ro, Buk-gu, Gwangju, Korea

[‡]Department of Materials Science and Engineering, Korea Advanced Institute of Science and Technology (KAIST), 291 Daehak-ro, Yuseong-gu, Daejeon, Korea

[§]Department of Chemical Engineering, Pohang University of Science and Technology (POSTECH), 77 Cheongam-ro, Nam-gu, Pohang, Korea

S Supporting Information

ABSTRACT: A precise control of the size, density, and distribution of metal nanoparticles dispersed on functional oxide supports is critical for promoting catalytic activity and stability in renewable energy and catalysis devices. Here, we measure the growth kinetics of individual Co particles ex-solved on SrTi$_{0.75}$Co$_{0.25}$O$_{3-\delta}$ polycrystalline thin films under a high vacuum, and at various temperatures and grain sizes using in situ transmission electron microscopy. The ex-solution preferentially occurs at grain boundaries and corners which appear essential for controlling particle density and distribution, and enabling low temperature ex-solution. The particle reaches a saturated size after a few minutes, and the size depends on temperature. Quantitative measurements with a kinetic model determine the rate limiting step, vacancy formation enthalpy, ex-solution enthalpy, and activation energy for particle growth. The ex-solved particles are tightly socketed, preventing interactions among them over 800 °C. Furthermore, we obtain the first direct clarification of the active reaction site for CO oxidation—the Co-oxide interface, agreeing well with density functional theory calculations.

INTRODUCTION

Ex-solution, an in situ growth of metal nanoparticles from parent complex oxide supports has attracted intense attention due to its potential applications in the fields of high-temperature catalysis and renewable energy.[1−14] For the perovskite oxide (ABO$_3$) which has been studied most intensively, transition or precious metals are incorporated into the B site of the perovskite lattice under oxidizing conditions, and they are egressed from the support upon subsequent reduction. Nanoparticle synthesis using this phenomenon offers exceptional capabilities for inhibiting the agglomeration of the particles during growth by anchoring them onto the surface of the perovskite support and for distributing them rather uniformly on the support, thereby becoming a candidate for overcoming the drawbacks of the conventional dispersion methods.[15−17]

A judicious control over the number, size, and distribution of ex-solved particles, a prerequisite for further improving the catalytic activity and stability, can only be achieved by understanding the kinetics of individual particle growth at varied parameters of ex-solution. Yet to date, this has not been explored, largely due to the limitations of post growth

analyses.[1−3,5−18] In situ transmission electron microscopy (TEM) offers such insights at subnanometer scale spatial resolution as evidenced by the study of Co ex-solution on Pr$_{0.5}$Ba$_{0.5}$Mn$_{0.9}$Co$_{0.1}$O$_{3-\delta}$ surfaces, which to our knowledge is the only report.[4] However, this study is limited to simply confirming the presence of a few sporadically scattered Co particles, which are extracted on uneven surfaces of Co-doped Pr$_{0.5}$Ba$_{0.5}$MnO$_3$ porous support in a severe reducing environment.

Here, we use in situ TEM to provide direct insights into the growth mechanism and kinetics of Co particles ex-solved on polycrystalline SrTi$_{0.75}$Co$_{0.25}$O$_{3-\delta}$ (STC) thin films under a high vacuum (1 × 10^{-7} Torr) and at varied temperatures (500−800 °C). The particle is extracted preferentially at grain boundaries and corners within our experimental condition (potentially lowering the ex-solution temperature), contrary to the ex-solution on other oxide systems.[1−18] Interestingly, the particle size increases with time until it reaches a critical radius at which it remains constant, and the radius depends on the

locations and temperature. Direct measurements of the particle size, combined with a theoretical model, allow us to determine the rate limiting step for growth, which is the finite supply of Co, and to estimate the Co vacancy formation and ex-solution energies (i.e., enthalpy), and the activation energy for growth. Remarkably, the particle coarsening is restricted up to 800 °C due to the stable nucleation sites on which the particle is strongly anchored. However, the three energy barriers vary with the sites, whose free energies are sensitive to the orientation, shape, and size of nearby grains. The uniform particle and grain size distributions over the entire range of the polycrystalline STC film enable us to identify that the active reaction site for CO oxidation is the interface of the Co particle on the oxide support. This is the first attempt to directly determine the presence of strong metal−support interactions that accelerate the reactivity of a real application using ex-solved catalysts. We find that this result is consistent with DFT calculations.

■ RESULTS AND DISCUSSION

A time series of TEM bright field (BF) images of the Co particles ex-solved from a STC thin film is extracted from a video obtained at 800 °C and 1×10^{-7} Torr, as shown in Figure 1a−d. The film is very thin (~25 nm), and it is a
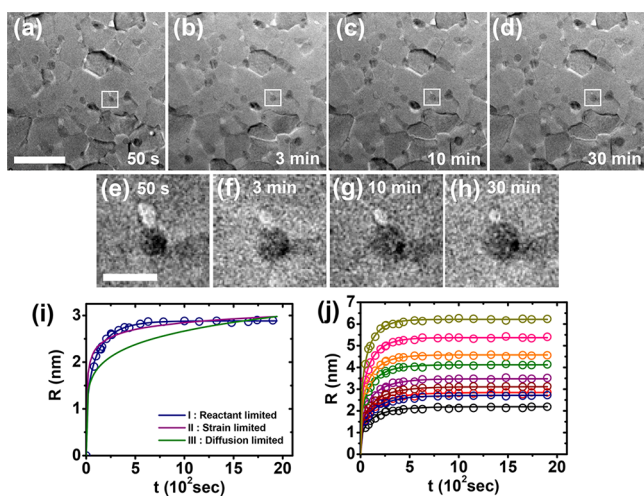

Figure 1. Real time observation of ex-solution of Co particles on a STC film during annealing at 800 °C with the fits to the kinetic data. (a−d) A series of TEM BF images of the Co particles with time. The scale bar is 50 nm. (e−h) A representative sequence of the images of a Co particle marked by boxes in (a−d). The time at which each image was taken is indicated in the image. The scale bar is 10 nm. (i,j) Plots of radius r versus time t of the particle in (e−h) and the selected particles in (a−d). Approximating the particle image by an ellipse, the radius r is calculated as the geometric mean of the semimajor and semiminor axes; that is, the radius of a circle with an equivalent area. In (i), the blue, purple, and green plots describe reactant limited, strain limited, and diffusion limited models, respectively.

polycrystal with a grain size ranging from 12 to 40 nm, and the size distribution was constant during annealing as shown in Figure S1. Most Co particles with darker contrasts are observed at grain boundaries and corners that are energetically favorable locations to minimize their nucleation energy barriers because these sites have higher free energies than other sites such as grain surfaces, and they are geometrically attractive sites where nuclei effectively consume defective sites.[19]

The high resolution transmission electron microscopy (HRTEM) image of a single Co particle created at a grain corner is shown in Figure 2a, and the fast Fourier transform
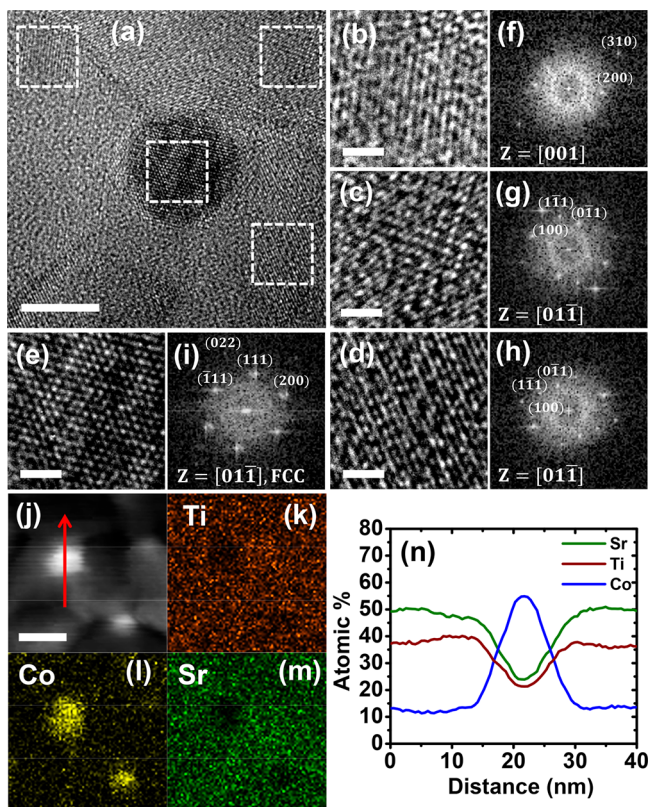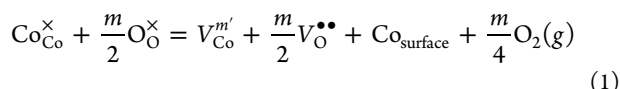

Figure 2. Identification of the Co particle ex-solved from the STC support. (a) A HRTEM image of a representative Co particle ex-solved at a grain corner. The scale bar is 5 nm. (b−e) Magnified images of the boxed regions in (a): The first three images of the STC are taken from the grains at left, right, and bottom, respectively. The last image of the Co is taken from the Co particle. The scale bar is 1 nm. (f−i) The corresponding FFT patterns of (b−e). (j) A STEM image for the two Co particles ex-solved at the grain corner and boundary. The scale bar is 20 nm. The red arrow indicates the direction to which the EDX line scan was performed. (k−m) EDX mapping images of Ti, Co, and Sr, respectively. (n) Data plots of the EDX line scan as indicated in (j).

(FFT) patterns of the boxed regions in Figure 2a are exhibited in Figure 2f−i with their magnified portions in Figure 2b−e. The HRTEM image was acquired while annealing the sample at 800 °C. The FFTs in Figure 2f−h and 2i were obtained for the three grains and the Co particle, respectively. We find that the crystal structure of the particle (and other particles in other locations) is face centered cubic (FCC), and the lattice spacings of (111) and (200) are 0.201 and 0.174 nm, respectively, in agreement with a pure Co crystal.[20] The FCC structure is thermodynamically preferred above 450 °C.[21−25] It is also found that the surrounding grains have a tetragonal structure and are aligned in different orientations as indicated by the FFT patterns. A nanoprobe-EDX line scan and an elemental mapping were also performed to measure the compositions of the Co particle and the STC film as presented in Figure 2j−n. The concentration of Co in the particle is considerably higher than that in the substrate film, suggesting that the nanoparticle is pure Co metal.

Figure 1e−h show a representative sequence of the magnified images of a Co particle marked by boxes in Figure 1a−d, and Figure 1i,j show quantitative measurements of the radius r (defined in the figure caption) versus the time t of this and several other particles with different sizes in Figure 1a−d, respectively. The size of the Co particle increases with time, but after approximately 10 min it remains constant. The particle has a saturated radius of 2.1−6.4 nm with an approximately round shape as shown in Figure 1g,h.

The Co ex-solution on the oxide surface is related with the partial Schottky defect formation in perovskite lattices.[26,27] To form the metallic Co on the surface, Co and O in the oxide lattice must be pulled out together while releasing O_2 gas, as illustrated in eq 1 (see the equation for full reaction process in Supporting Information):

$$Co_{Co}^{\times} + \frac{m}{2}O_O^{\times} = V_{Co}^{m'} + \frac{m}{2}V_O^{\bullet\bullet} + Co_{surface} + \frac{m}{4}O_2(g) \tag{1}$$

Here, $Co_{Co}^{\times}$ and $O_O^{\times}$ are cobalt and oxygen ions in the perovskite lattice, respectively. $V_{Co}^{m'}$ (m is an integer indicating the valence state of Co) and $V_O^{\bullet\bullet}$ are the cobalt and oxygen vacancies, respectively, and $Co_{surface}$ is a neutral Co segregated at the surface. A recent paper[18] reported that the ex-solution of Ni atoms on the $La_{0.4}Sr_{0.4}Sc_{0.9}Ni_{0.1}O_{3-\delta}$ (LSSN) surface was analyzed analytically and experimentally with ex situ experiments that focused on the analysis of the average sizes of ex-solved particles. Three limiting cases can be distinguished, in which the rate of the ex-solved particle growth is limited by one of the following factors: strain between the particle and host material, a limited supply of the ex-solved element, and diffusion through the inside and surface of the host material.

A summary of the three different models is provided in ref 18, and the best fits to our experimental data are plotted in Figure 1i. It is evident that the reactant-limited model excellently describes the data. We therefore focus on this case. Its theoretical model, which is modified to reflect our unique ex-solution conditions, can be written as follows (see the full derivation in SI 1, Supporting Information):

$$r = r_{r-lim}\left(1 - \exp\left(-\frac{t}{\tau_{r-lim}}\right)\right)^{1/3} \tag{2}$$

Here, $r_{r-lim} = \left(\frac{V_b}{\rho}([Co_{Co}^{\times}]_0 - [Co_{Co}^{\times}]_{eq})\right)^{1/3} = \left(\frac{V_b}{\rho}[V_{Co}^{m'}]_{eq}\right)^{1/3}$ and $\tau_{r-lim} = \frac{V_b}{\rho v_0}$ where V_b is the volume of the support being analyzed, ρ is the molar density of Co metal, $[Co_{Co}^{\times}]_0$ is the initial concentration of Co ions in the STC before ex-solution, $[Co_{Co}^{\times}]_{eq}$ and $[V_{Co}^{m'}]_{eq}$ are the equilibrium concentrations of Co ions and Co vacancies in the STC at temperature dependent reducing conditions, respectively, and v_0 is the prefactor involving all constants including the particle shape, and it is also thermally activated for evolving the particle including the activation energies for the strain between the particle and the STC film and the diffusion through the STC film. The two parameters controlling the kinetics of the ex-solved particle in eq 2 are thus r_{r-lim} and τ_{r-lim}, allowing us to directly determine the values of the subcomponents and their dependence on temperature. τ_{r-lim} is fitted to the initial increase in the particle size, describing the sharpness of the saturation point, and r_{r-lim} is fitted to the final regime, determining the saturated size of the particle. We emphasize that our modified model is

distinguished from one in ref 18 in that the r_{r-lim} is not decided by $[Co_{Co}^{\times}]_0$ but by $[V_{Co}^{m'}]_{eq}$, which depends on temperature, because our system is under high vacuum conditions.

We measured all the 54 ex-solved particle growth events at 800 °C as shown in Figure 1a−d and 16, 43, and 64 growth events at 500, 600, and 700 °C, respectively, as shown in Figure 3a−c. The selected sets of data and fits to eq 2 are
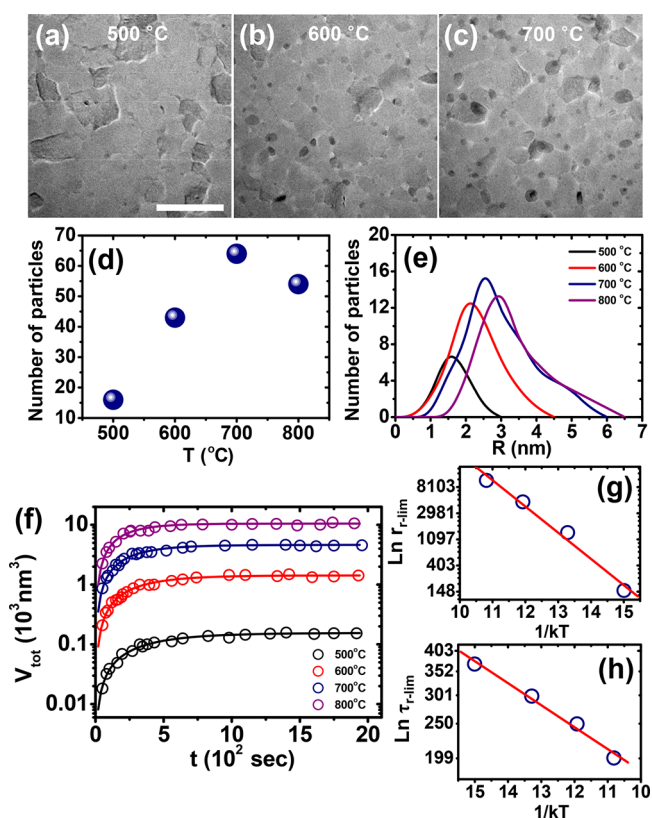

Figure 3. Real time observation of Co particles ex-solved at other temperatures with statistical and kinetic analyses. (a−c) The BF images of the Co particles on the STC films after their sizes are saturated at 500, 600, and 700 °C, respectively. The scale bar is 50 nm. (d) A plot of the number of ex-solved particles as a function of temperature. (e) Plots of particle size distributions at varied temperatures. (f) Fits to the data plots of the total volume of the ex-solved Co particles with time. The data were collected from the specified areas (2.3×10^4 nm^2) of the STC films in (a−c) and Figure 1a−d. (g,h) Arrhenius plots of the fitted parameters of r_{r-lim} and τ_{r-lim}, respectively.

shown in Figure 1j for 800 °C and in Figure S2 for the other temperatures. After fitting each curve independently, we find that the resulting values of r_{r-lim} and τ_{r-lim} vary between the particles at a given temperature as shown in Table 1; the particle with a larger saturated size is fitted by the larger value of r_{r-lim} and the smaller value of τ_{r-lim}. Such a deviation in the values of these two parameters might depend on the site at which each particle is ex-solved. It is possible that each site has a different surface, grain boundary, or grain corner energy depending on the orientation, shape and size of nearby grains. This tendency gives rise to the variation in the formation energy for $V_{Co}^{m'}$ and the activation energy for v_0, both of which determine the two fitting parameters and ultimately the size distribution of the ex-solved particles. Note that V_b and ρ are

Table 1. Values of Fitted Parameters for the Particles of Different Sizes at Various Temperatures for Ex-solution[a]

500 °C			600 °C			700 °C			800 °C		
$r_{saturated}$	r_{r-lim}	T_{r-lim}	$r_{saturated}$	r_{r-lim}	T_{r-lim}	$r_{saturated}$	r_{r-lim}	T_{r-lim}	$r_{saturated}$	r_{r-lim}	T_{r-lim}
1.26	1.26	400	1.18	1.18	300	1.70	1.70	300	2.18	2.18	220
1.56	1.56	370	1.84	1.83	270	2.33	2.32	270	2.72	2.71	230
1.63	1.63	340	2.30	2.27	240	2.68	2.67	250	2.84	2.84	240
1.79	1.78	300	2.92	2.88	200	3.20	3.22	230	3.12	3.10	220
2.14	2.14	230	3.51	3.47	150	3.42	3.42	220	3.51	3.47	200
			3.82	3.80	120	3.72	3.73	200	4.13	4.12	170
						4.09	4.12	180	4.55	4.57	160
						4.54	4.52	150	5.40	5.37	150
									6.23	6.21	130

[a] The units of $r_{saturated}$ and r_{r-lim} are nm, and that of τ_{r-lim} is second.

constant, independent of the ex-solution sites. Importantly, each particle with a different size is fitted by a set of the two parameters over 30 min for growth, indicating particle growth dominates over particle interactions. Such excellent particle stability should be ascribed to the stable ex-solution sites (within our experimental conditions) at which the particle can be tightly anchored up to 800 °C. Considering that most of the particles nucleate before the time (~30 s) when we start to observe the ex-solution event, and the fits of the data, most of the particles nucleate within a narrow range of times.

We now discuss the temperature dependence of the ex-solution of Co metal. As shown in Figure 3a, ex-solution occurs at temperatures as low as 500 °C and at 1×10^{-7} Torr. Such a low temperature ex-solution is probably induced by the high vacuum (thus the low oxygen partial pressure, 2.64×10^{-11} atm) in TEM, and the energetically efficient nucleation sites at the grain boundaries and corners, which should significantly reduce the vacancy formation energy (thus the ex-solution energy) and the nucleation energy barriers.[19] We performed the experiment isothermally at each designated temperature with a different sample. The images in Figure 3a–c show the ex-solved Co particles whose sizes are saturated at 500, 600, and 700 °C, respectively, and we did not observe particle coarsening afterward. The grain size distributions at the three temperatures are nearly similar as shown in Figure S3.

The number of ex-solved particles and size distributions are plotted with temperature as shown in Figure 3d,e, respectively. The former increases with temperature but after 700 °C, it decreases. The latter presents near Gaussian distributions with an increasing mean particle radius and a larger standard deviation in the radius as temperature increases. However, after 700 °C, the standard deviation in the radius is nearly unchanged, whereas the mean radius increases. These statistics imply that at temperatures above 700 °C, the ex-solved Co atoms diffuse onto the existing particles rather than nucleating new ones at grain boundaries or corners because such high temperatures increase the diffusivity of the Co atom and the distances between the particles previously nucleated are shortened. We also observed that as the average grain size increases, the particle density decreases, while the average particle size remains nearly constant, reflecting that the total amount of ex-solved Co atoms decreases at a given temperature (Figure S4d–f). These results suggest that the Co atoms are preferentially extracted at grain boundaries and corners; thus, the density and distribution of the particle is controlled by the grain sizes of the film, while the size of the particle is primarily determined by temperature.

To further analyze the physical significance of the fitting parameters as a function of temperature, we measured the total volume of the ex-solved particles in a specified area (2.3×10^4 nm^2) of the STC film with time at varied annealing temperatures. Figure 3f shows the temperature dependence of the total volume of Co in which each plot is obtained from the images in Figure 3a–c and Figure 1c,d. As expected, the data are well fitted by an extended form[28] of volume based on eq 2, and from this, the two fitting parameters are extracted at different temperatures. The parameters also scale with the saturated total volume of the particle in the same manner as those of individual particles as discussed above. Thus, the values of the fit allow us to find the Co vacancy formation enthalpy (1.0 eV) and the activation energy (0.14 eV) for growth of the particle as shown in Figure 3g,h, respectively. Additionally, by defining the equilibrium constant for the Co ex-solution described in eq 1, we find that the enthalpy for this ex-solution reaction is larger than the Co vacancy formation enthalpy by a factor of $(2 + m)/2$ (see SI 2 in Supporting Information). Generally, Co exists in the mixed valence states of 2+ and 3+ in a perovskite lattice,[29,30] implying that the enthalpy for the ex-solution reaction is 2–2.5-fold larger than the enthalpy for the Co vacancy formation.

To characterize the catalytic performance of the Co particle ex-solved on the STC support, the oxidation of CO was investigated at various temperatures (100–250 °C). We discovered that most of the Co particles are hexagonal close packed (HCP)[20] at room temperature in TEM, as indicated by the HRTEM and FFT of a representative Co particle as shown in Figure S5. It is reasonable to assume that the FCC Co particles created during annealing transforms to the HCP Co at room temperature because HCP Co is stable below 450 °C.[21-25] Figure 4a shows the CO conversion ratio as a function of the reaction temperature. It is apparent that the sample reduced at higher temperature converts more CO molecules over the entire range of reaction temperatures due probably to the amount of ex-solved Co atoms, which increases sensitively to preannealing temperature as shown in Figure 3f.

To verify the active site for the formation of CO$_2$, we examined the turnover frequencies (TOFs) as a function of the reaction temperatures, as shown in Figure 4b. The TOFs were obtained at different geometric locations of the Co particles ex-solved at various temperatures. Direct measurements of the Co particle using TEM allow us to estimate the number of sites (number of Co atoms) at the perimeter, surface and volume in the entire area of the sample. This approach can be reasonably adopted because the size distributions of the Co particles at different locations in the STC layer are nearly identical (see
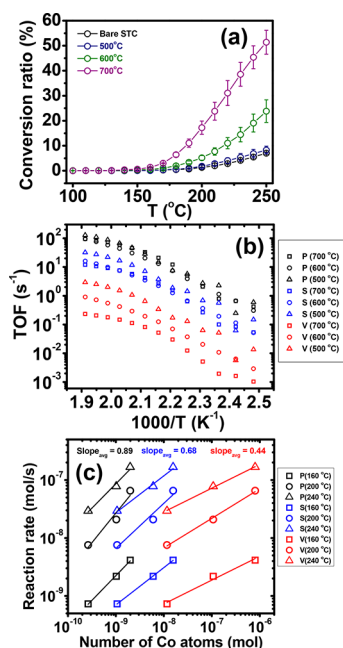
Figure 4. Characterization of CO oxidation properties of the ex-solved Co particles on the STC support. (a) A plot of CO conversion ratio vs reaction temperature. (b) An Arrhenius plot of turnover frequencies (TOFs) at different geometries (i.e., perimeter at the junction where the Co particle, the STC support, and the gas meet, surface area of the Co particle, and the volume of the Co particle; the three geometries are denoted as P, S, and V in plots) of the Co particles ex-solved at various temperatures (i.e., 500, 600, and 700 °C), which are labeled in the legend. (c) A plot of reaction rate vs number of Co atoms at different particle geometries for various reaction temperatures (i.e., 160, 200, and 240 °C as labeled in the legend) of CO oxidation. The three geometries are also denoted as P, S, and V with different colors of black, blue, and red in plots, respectively. Each plot includes three data points; the data of the smallest number of Co atoms was obtained from the sample where Co atoms were ex-solved at 500 °C, the data in the middle at 600 °C, and the data in the largest at 700 °C.

Figure S6a−c), due to the consistent size distributions of grains at those locations (see Figure S6d−f). We confirmed that this trend persisted at the three ex-solution temperatures at which different amounts of Co atoms are ex-solved and different size distributions of Co particles appear. From these plots, we find that when the reaction rate is normalized by the Co atoms at the perimeter of the particle (where the particle, support and gas meet), the samples annealed at the three temperatures, exhibit the most equivalent TOF values compared to the other cases, indicating that the atoms at the interface of the particle on the support are the dominant active sites for CO oxidation. The active site can be analytically confirmed by evaluating the TOF at different geometric sites as presented in Figure 4c. At the perimeter of the particle, the slope of the plot of reaction rate vs number of Co atoms is closest to unity, representing nearly constant TOF values regardless of the various size distributions of particles, the amount of Co atoms and the reaction temperatures. We note that this is the first determination of the strong metal−support interaction occurring in the system of ex-solved catalysts.

To explain how the interface of the Co nanoparticle on the STC support acts as the dominant reaction site for CO oxidation, we performed density functional theory (DFT) calculations based on the Mars−van Krevelen (MvK)

mechanism[31,32] (see the details in Experimental Section). This mechanism suggests four elementary steps for the CO oxidation reaction: CO adsorption, CO_2 formation leaving a surface oxygen vacancy, O_2 adsorption into the oxygen vacancy, and CO_2 formation via the reaction of another adsorbing CO and the adsorbed O_2 with the clean surface retrieved. Through this consecutive oxidation process, two CO molecules and one O_2 molecule are converted into two CO_2 molecules on oxide surfaces. The effect of ex-solved Co on the activity of CO oxidation is illustrated by the relative energy diagrams for the three different forms of Co atoms for CO oxidation (Figure 5a), with the schematics depicting the
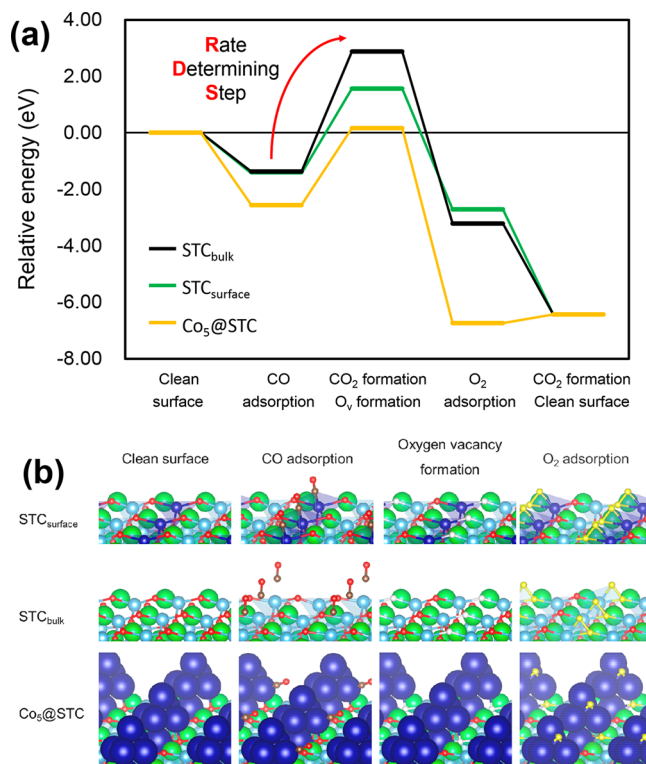

Figure 5. Density functional theory (DFT) calculations of CO oxidation at Co particles on STC films. (a) Relative energy diagram of CO oxidation on $STC_{surface}$, STC_{bulk}, and Co_5@STC. (b) Optimized structures of reaction intermediates during the CO oxidation at each elementary step on $STC_{surface}$, STC_{bulk}, and Co_5@STC. White and yellow atoms represent oxygen vacancy and adsorbed O_2, respectively. To identify adsorption sites on Co_5@STC more clearly, we present the ex-solved Co NP with a larger Co than that of $STC_{surface}$ and STC_{bulk}.

reaction at each step (Figure 5b). STC_{bulk}, $STC_{surface}$, and Co_5@STC represent Co located in bulk and on the surface of the oxide, and a Co NP anchored on the film, respectively. This diagram shows that the first CO_2 formation step has the largest energy barrier, and is thus the rate-determining step (RDS) of the overall reaction. At the RDS, the adsorbed CO reacts with the lattice oxygen of STC to form a CO_2 molecule by creating a surface oxygen vacancy. Then, an absorbed O_2 molecule is dissociated to migrate onto the Co NP and the oxygen vacancy of the STC surface. We find that the adsorption energy of CO (E_{CO}), the oxygen vacancy formation energy (E_{vf}), the energy barrier at the RDS, and the adsorption energy of the O_2 molecule (E_{O2}) are the lowest for Co_5@STC (see Table 2). This indicates that the interface between the Co

particle and STC is the most reactive site for CO oxidation, consistent with the experimental results.

Table 2. Adsorption Energies (eV) of CO on a Clean Surface (E_{CO}) and O_2 into a Surface Oxygen Vacancy (E_{O2}) on $STC_{surface}$, STC_{bulk}, and $Co_5@STC^a$

	E_{vf}	E_{CO}	E_{O2}	E_{RDS}
STC_{bulk}	6.09	−1.38	−6.10	4.25
$STC_{surface}$	4.78	−1.44	−4.29	3.00
$Co_5@STC$	3.38	−2.56	−6.90	2.72

$^a E_{vf}$ and E_{RDS} are the formation energy of an oxygen vacancy and the required energy for rate determining step, respectively.

CONCLUSIONS

Quantitative in situ measurements combined with a theoretical model provide the key information on the factors controlling the size and distribution of the ex-solved Co catalysts by simply changing the temperature, and the grain sizes of the polycrystalline oxide supports at a low pressure in a TEM. Such conditions can be extended to different vacuum/reducing environments (in other systems) by tuning the parameters of ex-solution such as oxygen partial pressure, temperature, grain size, doping concentration, film thickness, etc., which are compensated to one another. Thus, our results are reproducible in other systems and highly practical for real applications. Moreover, the uniform size distributions of the ex-solved catalysts on supporting polycrystalline films with precise measurements of the particle sizes at subnanometer scale spatial resolution could serve as an effective route for identifying the active sites of catalysts on various oxide supports. Our approach to seek the active site is novel because it is not eligible for the porous bulk oxide supports[1−18] with uneven surfaces where consistent particle size distributions are not achievable, and for thick polycrystalline films[7,45−47] with large grains where particle coarsening is severe and many ex-solved particles are buried in internal grain boundaries.

EXPERIMENTAL SECTION

Sample Preparation. $SrTi_{0.75}Co_{0.25}O_{3-\delta}$ (STC) thin films were grown onto SiO_2 membrane TEM grids (3 mm in diameter, TEM windows) for TEM analyses and onto 2 in.-sized Si wafers for CO oxidation tests via pulsed laser deposition (PLD) from an oxide target. The STC powders were synthesized via a conventional solid-state method from $SrCO_3$ (Sigma-Aldrich, 99.99%), TiO_2 (Sigma-Aldrich, 99.8%), and Co_3O_4 (Alfa Aesar, 99.7%) precursors with the desired Sr:Ti:Co stoichiometric ratios (1.00:0.75:0.25) and calcined in air at 1200 °C for 8 h with heating and cooling rates of 4 °C/min. The pellet-type STC target for PLD was prepared by uniaxial pressing followed by cold isostatic pressing at 200 MPa before the sintering process at 1350 °C for 8 h with heating and cooling rates of 4 °C/min. The PLD (VTS Corporation) was performed with a KrF excimer laser (Coherent COMPex Pro 205) operating at a wavelength of 248 nm with a repetition rate of 2 Hz during 5 min and a laser energy of 280 mJ/pulse. The samples were kept at 700 °C during deposition, while the oxygen pressure was maintained at 10 mTorr after pumping the background pressure to 10^{-5} Torr. After deposition, the samples were annealed at 700 °C for 20 min in 1 Torr of oxygen pressure in a chamber before cooling. The thickness of the resulting STC films was approximately 25 nm.

Analyses. The crystal structures of STC thin films and ex-solved Co particles were examined via high resolution transmission electron microscopy (HRTEM) and fast Fourier transformation (FFT) using a high resolution transmission electron microscope (TEM, Tecnai G2,

F30 S-Twin, operating at 80−300 keV, FEI). The elemental line scan and mapping of the particle were conducted by energy dispersive X-ray spectroscopy (EDX) and scanning transmission electron microscopy (STEM) with which our TEM were equipped. Investigation of the evolution and growth of the Co particle ex-solved on the STC film was conducted using an in situ heating holder (652 double tilt, Gatan) within our TEM (1×10^{-7} Torr). Each targeted temperature was reached in less than 30 s using an autocontrol mode depending on the targeted temperatures.

Catalytic Test for CO Oxidation. The catalytic activities for CO oxidation were evaluated in a quartz reactor with a diameter of 0.5 in.. For each measurement, we prepared three STC wafers (2 in.) and annealed the wafers under the same conditions as in the in situ TEM analyses (the selected temperatures were 500, 600, and 700 °C; the pressure in the chamber was 1×10^{-7} Torr; and the thickness of the film was approximately 25 nm.) for 30 min. Then, the wafers were cleaved as small pieces and loaded between quartz wool layers. The reactants consisted of 1 vol % CO and 4 vol % O_2 balanced with Ar gas under a total flow rate of 50 mL/min. The reactants and products were monitored in real time with a quadrupole mass spectrometer (PFEIFFER Vacuum GSD320) connected to the outlet of the reactor. The light-off curves were obtained by increasing the reaction temperature with a ramping rate at 3 °C/min while feeding reactant gases. The CO conversion ratio (%) is defined as $100 \times (mol_{CO,in} - mol_{CO,out})/mol_{CO,in}$. The turnover frequency values were calculated by normalization of the produced CO_2 molecules per second with the number of Co atoms (the atoms at perimeter, surface and volume, respectively). The peak intensity of carbon monoxide was corrected by considering the contribution of the cracking fragment of CO_2 (11.4%) with the mass concentration determination mode.

Computational Details. We performed density functional theory (DFT) calculations using the Vienna ab initio simulation package (VASP).[33] Exchange-correlation energies were treated via the Perdew−Burke−Ernzerhof (PBE) functional based on the generalized gradient approximation (GGA).[34] A plane wave expansion with a cutoff of 400 eV was used with a $3 \times 3 \times 1$ Monkhorst−Pack k-point sampling of the Brillouin zone.[35] Gaussian smearing was used with a width of 0.1 eV to determine the partial occupancies. Geometry relaxations were conducted using a conjugate gradient algorithm until the forces on all unconstrained atoms were less than 0.03 eV/Å. We used GGA + U schemes with the effective U values of 3.40 and 4.36 eV to describe the localized nature of the 4d electrons of Co and Ti, respectively.[36,37]

Our calculations are based on the STC(110) which is the top surface of most of the grains in our experiments, where the ex-solved Co particles are mostly placed. (Figure S5). A (2×1) surface unit cell with a 5 layer slab thickness was used for STC(110), whereas a (2×2) surface unit cell with a 3 layer slab thickness was used for $Co_5@STC(110)$. A vacuum thickness of 25 Å (Figure S7) was used for both slab models. Such a way to investigate a representative plane of the polycrystalline support using DFT calculations is proven to provide an accurate description for catalytic reactions and the behavior of ex-solution in other planes typically follow the same trend.[38,39]

Because the BO-terminated surface of perovskite has accurately described the experimental results of B-metal ex-solution,[36,40] we also used the BO-terminated surface of STO(110). We compared the catalytic activities of CO oxidation on as-synthesized STC where Co is located in bulk (STC_{bulk}) and the initial state of Co ex-solved STC ($STC_{surface}$) where Co is only segregated toward the surface. For STC_{bulk} and $STC_{surface}$, we substituted a Ti atom with a Co atom in the fifth layer and at the top surface layer of STO(110), respectively. For the ex-solved Co NPs on STC, the exact atomic structures are still unclear. On the basis of our experimental results, the ex-solved Co atoms finally become Co nanoparticles (NPs) on the STC surface with the several socketed atoms in the STC lattice. Since ex-solution occurs through the surface segregation of Co atoms in STC, some of Co atoms might remain near the surface of STC even after the formation of ex-solved NPs. For this, we substituted one B-site Ti of STO(110) with Co, which is similar to $STC_{surface}$. Then, we loaded the Co_5 cluster on STC surface as an exposed shape of the ex-solved

NP. Although larger size of cluster model is more realistic to describe experimentally observed NPs, using minimum size of metallic NPs takes advantage of reducing the computational cost for DFT calculations. In this regard, it has been demonstrated that even the cluster as small as Co_4 possesses a three-dimensional structure, where its metallic bonding was well described.[41] In addition, for a wide range of catalytic reactions such as CO poisoning on $Pd_4@CeO_2(111)$ in direct alcohol fuel cells,[42] CO_2 and H_2 adsorption on $Ni_5@YSZ(111)$ for reverse water gas shift reaction,[43] and CO and O_2 adsorption on $Pd_5@MgO(001)$, these small sizes of NPs can describe not only the effect of interface on molecular adsorption and oxygen vacancy formation on metal oxide surfaces, but also metal−support interaction.[43] In particular, DFT-calculated IR spectra of CO_2 adsorbed on $Ni_5@YSZ(111)$ showed good agreement with the experimental values.[43] Our DFT results demonstrated that the interface between ex-solved metal nanoparticle (Co_5) and support (STC) is the active site for CO oxidation, and it shows higher catalytic activity than bare STC (Figure 5a), which were also confirmed in our experiments. Therefore, we believe that Co_5 is sufficiently large to investigate CO oxidation on the ex-solved NPs supported by STC.

There are four symmetric 3-fold hollow sites near B-site atom at the surface of STC(110), so we constructed the most stable form of the 2 layer trigonal bipyramidal Co_5 clusters on STC(110)[44] (Figure S7). We examined molecular adsorption at four possible top (Co, O, Ti, and Sr) and three hollow (Sr−Ti−Sr, Ti, or Co−O−Sr) sites on STC(110) surface for CO and O_2 adsorptions, respectively. For $Co_5@STC(110)$, we additionally considered an interface between Co_5 and STC(110), top and hollow sites of Co_5. All of surface oxygen atoms were considered to search for the most preferred oxygen vacancy formation sites. The most stable configurations from each set of calculations were used (Figure 5b).

The oxygen vacancy formation energy (E_{vf}) was calculated from the total energy differences between the supercells with and without a surface oxygen vacancy;

$$E_{vf} = \left(E_{vac} + \frac{1}{2}E_{O2}\right) - E_{surf}$$

where E_{vac} is the total energy of the system with an oxygen vacancy, E_{O2} is the total energy of an isolated O_2 in the gas phase, and E_{surf} is the total energy of optimized clean surface structures. The adsorption energy (E_{ads}) is defined as the change in total energy due to the molecular adsorption at each surface:

$$E_{ads} = E_{A\text{-surf}} - E_{surf} - E_{A(gas)}$$

where $E_{A\text{-surf}}$ is the total energy of a molecule adsorbed on the surface and $E_{A(gas)}$ is the total energy of an isolated molecule in the gas phase. With our definition, a lower value of E_{vf} or E_{ads} indicates that the process is energetically preferred.

ASSOCIATED CONTENT

ⓢ Supporting Information

The Supporting Information is available free of charge on the ACS Publications website at DOI: 10.1021/jacs.9b01882.

> SI 1: A kinetic model for the growth of ex-solved Co particle under the reactant limited regime; SI 2: Defect chemistry of the Co ex-solution; Supporting References; Figures S1−S7 (PDF)

AUTHOR INFORMATION

Corresponding Authors
*wcjung@kaist.ac.kr
*kimbj@gist.ac.kr

ORCID ⓞ

Kyeounghak Kim: 0000-0003-1297-6038
Jeong Woo Han: 0000-0001-5676-5844
WooChul Jung: 0000-0001-5266-3795
Bong-Joong Kim: 0000-0002-5335-4342

Author Contributions

‖Y.-R.J. and B.K. are equally contributing authors.

Notes

The authors declare no competing financial interest.

REFERENCES

(1) Neagu, D.; Tsekouras, G.; Miller, D. N.; Ménard, H.; Irvine, J. T. S. In situ growth of nanoparticles through control of non-stoichiometry. *Nat. Chem.* **2013**, *5*, 916−923.

(2) Kwon, O.; Sengodan, S.; Kim, K.; Kim, G.; Jeong, H. Y.; Shin, J.; Ju, Y.-W.; Han, J. W.; Kim, G. Exsolution trends and co-segregation aspects of self-grown catalyst nanoparticles in perovskites. *Nat. Commun.* **2017**, *8*, 15967.

(3) Neagu, D.; Oh, T.-S.; Miller, D. N.; Menard, H.; Bukhari, S. M.; Gamble, S. R.; Gorte, R. J.; Vohs, J. M.; Irvine, J. T. S. Nano-socketed nickel particles with enhanced coking resistance grown in situ by redox exsolution. *Nat. Commun.* **2015**, *6*, 8120.

(4) Sun, Y.-F.; Zhang, Y.-Q.; Chen, J.; Li, J.-H.; Zhu, Y.-T.; Zeng, Y.-M.; Amirkhiz, B. S.; Li, J.; Hua, B.; Luo, J.-L. New opportunity for in situ exsolution of metallic nanoparticles on perovskite parent. *Nano Lett.* **2016**, *16*, 5303−5309.

(5) Myung, J.; Neagu, D.; Miller, D. N.; Irvine, J. T. S. Switching on electrocatalytic activity in solid oxide cells. *Nature* **2016**, *537*, 528−531.

(6) Irvine, J. T. S.; Neagu, D.; Verbraeken, M. C.; Chatzichristodoulou, C.; Graves, C.; Mogensen, M. B. Evolution of the electrochemical interface in high-temperature fuel cells and electrolysers. *Nat. Energy* **2016**, *1*, 1.

(7) Katz, M. B.; Zhang, S.; Duan, Y.; Wang, H.; Fang, M.; Zhang, K.; Li, B.; Graham, G. W.; Pan, X. Reversible precipitation/dissolution of precious-metal clusters in perovskite-based catalyst materials: Bulk versus surface re-dispersion. *J. Catal.* **2012**, *293*, 145−148.

(8) Zhu, Y.; Zhou, W.; Chen, Y.; Yu, J.; Xu, X.; Su, C.; Tade, M. O.; Shao, Z. A new cathode for solid oxide fuel cells capable of in situ electrochemical regeneration. *J. Mater. Chem.* **2011**, *21*, 15343−15351.

(9) Gao, Y.; Wang, J.; Lyu, Y.-Q.; Lam, K.; Ciucci, F. In situ growth of Pt3Ni nanoparticles on an A-site deficient perovskite with enhanced activity for the oxygen reduction reaction. *J. Mater. Chem. A* **2017**, *5*, 6399−6404.

(10) Zhou, W.; Shao, Z.; Liang, F.; Chen, Z.-G.; Zhu, Z.; Jin, W.; Xu, N. Boosting oxygen reduction reaction activity of palladium by stabilizing its unusual oxidation states in perovskite. *Chem. Mater.* **2015**, *27*, 3048−3054.

(11) Kwak, N. W.; Jeong, S. J.; Seo, H. G.; Lee, S.; Kim, Y.; Kim, J. K.; Byeon, P.; Chung, S.-Y.; Jung, W. Heterogeneous doping, a novel in-situ synthesis of supported metal nanocatalysts. *Nat. Commun.* **2018**, *9*, 4829.

(12) Xu, X.; Wang, W.; Zhou, W.; Shao, Z. Recent Advances in Novel Nanostructuring Methods of Perovskite Electrocatalysts for Energy-Related Applications. *Small methods* **2018**, *2* (7), 1800071.

(13) Song, Y.; Wang, W.; Ge, L.; Xu, X.; Zhang, Z.; Julião, P. S. B.; Zhou, W.; Shao, Z. Rational Design of a Water-Storable Hierarchical Architecture Decorated with Amorphous Barium Oxide and Nickel Nanoparticles as a Solid Oxide Fuel Cell Anode with Excellent Sulfur Tolerance. *Adv. Sci.* **2017**, *4* (11), 1700337.

(14) Gao, Y.; Lu, Z.; You, T. L.; Wang, J.; Xie, L.; He, J.; Ciucci, F. Energetics of Nanoparticle Exsolution from Perovskite Oxides. *J. Phys. Chem. Lett.* **2018**, *9*, 3772−3778.

(15) Kim, S.; Jun, A.; Kwon, O.; Kim, J.; Yoo, S.; Jeong, H. Y.; Shin, J.; Kim, G. Nanostructured double perovskite cathode with low sintering temperature for intermediate temperature solid oxide fuel cells. *ChemSusChem* **2015**, *8*, 3153–3158.

(16) Gorte, R. J.; Vohs, J. M. Nanostructured anodes for solid oxide fuel cells. *Curr. Opin. Colloid Interface Sci.* **2009**, *14*, 236–244.

(17) Schlupp, M. V. F.; Evans, A.; Martynczuk, J.; Prestat, M. Micro-solid oxide fuel cell membranes prepared by aerosol-assisted chemical vapor deposition. *Adv. Energy Mater.* **2014**, *4*, 1301383.

(18) GaO, Y.; Chen, D.; Saccoccio, M.; Lu, Z.; Ciucci, F. From material design to mechanism study: Nanoscale Ni exsolution on a highly active A-site deficient anode material for solid oxide fuel cells. *Nano Energy* **2016**, *27*, 499–508.

(19) Porter, D. A.; Easterling, K. E. *Phase Transformations in Metals and Alloys*, 2nd ed.; Chapman & Hall, 1992.

(20) JCPDS 79−0176 (STO), JCPDS 05−0727 (HCP), and JCPDS 15−0806 (FCC).

(21) Kitakami, O.; Sato, H.; Shimada, Y.; Sato, F.; Tanaka, M. Size effect on the crystal phase of cobalt fine particles. *Phys. Rev. B: Condens. Matter Mater. Phys.* **1997**, *56*, 13849–13854.

(22) International Centre for Diffraction Data, *Powder Diffraction File 1994, PDF-2 Database Sets 1−44*; International Centre for Diffraction Data: Pennsylvania, PA, 1994.

(23) Dinega, D. P.; Bawendi, M. G. A solution-phase chemical approach to a new crystal structure of cobalt. *Angew. Chem., Int. Ed.* **1999**, *38*, 1788–1791.

(24) Huang, J. Y.; Wu, Y. K.; Ye, H. Q. Phase transformation of cobalt induced by ball milling. *Appl. Phys. Lett.* **1995**, *66*, 308–310.

(25) Ericsson, T. The temperature and concentration dependence of the stacking fault energy in the Co-Ni system. *Acta Metall.* **1966**, *14*, 853–865.

(26) Schmalzried, H. Internal and external oxidation of nonmetallic compounds and solid solutions (I). *Phys. Chem.* **1983**, *87*, 551–558.

(27) Koo, B.; Kwon, H.; Kim, Y. J.; Seo, H. G.; Han, J. W.; Jung, W. C. Enhanced oxygen exchange of perovskite oxide surfaces through strain-driven chemical stabilization. *Energy Environ. Sci.* **2018**, *11*, 71–77.

(28) $V = \frac{4}{3}\pi r_{r-\lim}^3 \left(1 - \exp\left(-\frac{t}{\tau_{r-\lim}}\right)\right)$ where the particle is considered a sphere.

(29) Bi, L.; Kim, H.-S.; Dionne, G. F.; Ross, C. A. Structure, magnetic properties and magnetoelastic anisotropy in epitaxial $Sr(Ti_{1-x}Co_x)O_3$ films. *New J. Phys.* **2010**, *12*, 043044.

(30) Onbaşlı, M. C.; Goto, T.; Tang, A.; Pan, A.; Battal, E.; Okyay, A. K.; Dionne, G. F.; Ross, C. A. Oxygen partial pressure dependence of magnetic, optical and magneto-optical properties of epitaxial cobalt-substituted $SrTiO_3$ films. *Opt. Express* **2015**, *23*, 13399–13409.

(31) Kim, K.; Yoo, J. D.; Lee, S.; Bae, M.; Bae, J.; Jung, W. C.; Han, J. W. A Simple Descriptor to Rapidly Screen CO Oxidation Activity on Rare-Earth Metal-Doped CeO_2: From Experiment to First-Principles. *ACS Appl. Mater. Interfaces* **2017**, *9*, 15449–15458.

(32) Kim, K.; Han, J. W. Mechanistic study for enhanced CO oxidation activity on (Mn,Fe) co-doped CeO_2(111). *Catal. Today* **2017**, *82*, 293–294.

(33) Kresse, G.; Furthmüller, J. Efficient iterative schemes for *ab initio* total-energy calculations using a plane-wave basis set. *Phys. Rev. B: Condens. Matter Mater. Phys.* **1996**, *54*, 11169–11186.

(34) Grimme, S. Semiempirical GGA-type density functional constructed with a long-range dispersion correction. *J. Comput. Chem.* **2006**, *27*, 1787–1799.

(35) Monkhorst, H. J.; Pack, J. D. Special points for Brillouin-zone integrations. *Phys. Rev. B* **1976**, *13*, 5188–5192.

(36) Kwon, O.; Sengodan, S.; Kim, K.; Kim, G.; Jeong, H. Y.; Shin, J.; Ju, Y.-W.; Han, J. W.; Kim, G. Exsolution trends and co-segregation aspects of self-grown catalyst nanoparticles in perovskites. *Nat. Commun.* **2017**, *8*, 15967.

(37) Klyukin, K.; Alexandrov, V. Effect of intrinsic point defects on ferroelectric polarization behavior of $SrTiO_3$. *Phys. Rev. B: Condens. Matter Mater. Phys.* **2017**, *95*, 035301.

(38) Seo, M. H.; Park, H. W.; Lee, D. U.; Park, M. G.; Chen, Z. Design of highly active perovskite oxides for oxygen evolution reaction by combining experimental and ab Initio studies. *ACS Catal.* **2015**, *5*, 4337–4344.

(39) Lu, J.; Zhu, C.; Pan, C.; Lin, W.; Lemmon, J. P.; Chen, F.; Li, C.; Xie, K. Highly efficient electrochemical reforming of CH_4/CO_2 in a solid oxide electrolyser. *Sci. Adv.* **2018**, *4*, eaar5100.

(40) Kwon, O.; Kim, K.; Joo, S.; Jeong, H. Y.; Shin, J.; Han, J. W.; Sengodan, S.; Kim, G. Self-assembled alloy nanoparticles in a layered double perovskite as a fuel oxidation catalyst for solid oxide fuel cells. *J. Mater. Chem. A* **2018**, *6*, 15947–15953.

(41) Ha, N. N.; Ha, N. T.; Long, N. B.; Cam, L. M. Conversion of Carbon Monoxide into Methanol on Alumina-Supported Cobalt Catalyst: Role of the Support and Reaction Mechanism—A Theoretical Study. *Catalysts* **2019**, *9* (1), 6.

(42) Wen, C.; Wei, Y.; Tang, D.; Sa, B.; Zhang, T.; Chen, C. Improving the electrocatalytic properties of Pd-based catalyst for direct alcohol fuel cells: effect of solid solution. *Sci. Rep.* **2017**, *7*, 4907.

(43) Cadi-Essadek, A.; Roldan, A.; Aparicio-Angles, X.; Leeuw, N. H. d. CO_2 and H_2 Adsorption and Reaction at Ni_n/YSZ(111) Interfaces: A Density Functional Theory Study. *J. Phys. Chem. C* **2018**, *122*, 19463–19472.

(44) Aslan, M.; Davis, J. B. A.; Johnston, R. L. Global optimization of small bimetallic Pd−Co binary nanoalloy clusters: a genetic algorithm approach at the DFT level. *Phys. Chem. Chem. Phys.* **2016**, *18*, 6676–6682.

(45) Li, B.; Katz, M. B.; Duan, Y.; Du, X.; Zhang, K.; Chen, L.; Ven, A. V. d.; Graham, G. W.; Pan, X. A joint theoretical and experimental study of phase equilibria and evolution in Pt-doped calcium titanate under redox conditions. *Chem. Mater.* **2015**, *27*, 18–28.

(46) Kogler, S.; Nenning, A.; Rupp, G. M.; Opitz, A. K.; Fleig, J. Comparison of electrochemical properties of $La_{0.6}Sr_{0.4}FeO_{3-\delta}$ thin film electrodes: Oxidizing vs. reducing conditions. *J. Electrochem. Soc.* **2015**, *162*, F317–F326.

(47) Sengodan, S.; Ju, Y.-W.; Kwon, O.; Jun, A.; Jeong, H. Y.; Ishihara, T.; Shin, J.; Kim, G. Self-decorated MnO nanoparticles on double perovskite solid oxide fuel cell anode by *in Situ* exsolution. *ACS Sustainable Chem. Eng.* **2017**, *5*, 9207–9213.